Clean Energy, 2021, 673–689

https://doi.org/10.1093/ce/zkab040
Homepage: https://academic.oup.com/ce

Research Article

Daily, monthly and annual thermal performance of a linear Fresnel reflector to drive an organic Rankine-cycle system

Hassan Mahmood[1,*] and Khaled Hossin[2,3]

[1]Mechanical and Construction Engineering, University of Northumbria, Newcastle upon Tyne, UK
[2]Mechanical and Industrial Engineering Department, American University of Ras Al Khaimah, Ras Al Khaimah, United Arab Emirates
[3]Mechanical Engineering Department, University of Benghazi, Benghazi, Libya

*Corresponding author. E-mail: hassan.mahmood@northumbria.ac.uk

Abstract

The organic Rankine cycle (ORC) coupled with a linear Fresnel reflector (LFR) utilizes a low-grade heat source. This article presents the study of a small-scale LFR–ORC power-generation plant under the climatic conditions of Almatret, Spain. The mathematical modelling is performed using thermodynamic equations and simulations are conducted to evaluate the optical performance of the LFR system and thermal performance of the ORC plant. Therminol-62 is used as a heat-transfer fluid (HTF) in the solar field, whereas NOVEC™ 649 is used as the working fluid in the ORC power system. The LFR is integrated with a thermal-storage unit based on a two-tank system and stores the solar thermal energy via a heat exchanger. The thermal-energy output of the receiver tube of the LFR system is 108 kW and thermal losses are 7.872 kW during the peak time operation of a day at 1:00 p.m. The mechanical power output of the ORC turbine is 7.296 kW using the specific design conditions and the two-tank thermal-storage system adds 4 operation hours to the power plant after sunset.

Received: 14 May 2021; **Accepted:** 6 September 2021

Graphical Abstract

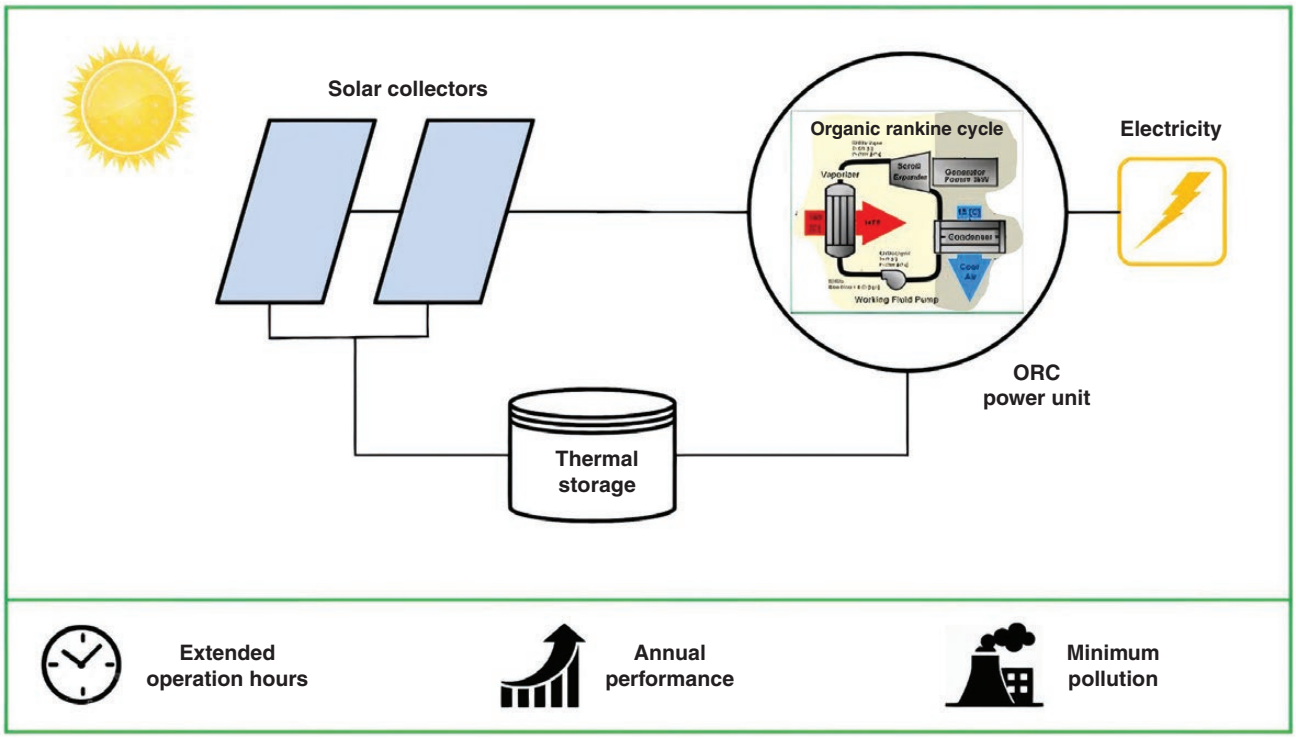

Keywords: solar energy; linear Fresnel reflector; energy storage; organic Rankine cycle

Introduction

Power generation using fossil fuel emits toxic carbon emissions into the environment. Renewable energy is an alternative solution to meet the world's growing demand for energy production and to reduce carbon-dioxide emissions. One of the most efficient solutions is using a low-grade heat source, such as biomass, geothermal, waste heat-source recovery and solar energy. The Rankine cycle uses the steam turbine to operate at high temperature and pressure, requiring a high-temperature source. In low-grade heat sources, the organic Rankine cycle (ORC) power plant is the most reliable and promising technology [1]. Tartiere *et al.* studied the ORC technology world market. The solar application contributes 1% of the total ORC globally installed capacity. The ORC heat source has different origins, such as waste heat from industries, biomass combustion, solar radiation or ground heat sources. In addition, refrigerants are used as working fluids instead of water. The selection of working fluid and operating conditions greatly affect the ORC energy efficiency [2]. Fig. 1 shows the schematic diagram and temperature–entropy (T–s) diagram of the simple ORC plant. The ORC is made of four processes in the evaporator, turbine, condenser and pump. The T–s diagram visualizes the heat contents of the cycle. The thermodynamic diagram of the ORC is similar to the conventional Rankine cycle and consists of four processes [3]:

- Process 1–2 is an isentropic expansion in the turbine, and work (W_T) is generated by the turbine.
- Process 2–3 is an isobaric condensation process, during which the heat (Q_{cond}) (in W) is rejected in the cycle.
- Process 3–4 is an adiabatic compression of the fluid in the pump (W_p) (in W).
- Process 4–1 involves an isobaric heat addition (Q_{evp}) to the system in the evaporator.

The selection of working fluid influences the performance of the ORC. Various studies have shown the thermal performance of the ORC using different types of refrigerants. Wang *et al.* studied the selection of working fluid for an ORC based on the environmental benefits and economic performance. Fourteen different fluids were analysed from temperature range of 90–230°C to determine the effect of the heat-source temperature on the greenhouse-gas emissions [4]. Tchanche *et al.* studied the effect of different types of working fluids for a low-grade heat-source ORC. The results showed that HCFC-134a, HCFC-152a, HCFC-600, HCFC-600a and HCFC-290 were the more suitable working fluids using the heat source of <90°C [5]. Santiago *et al.* investigated an ORC using five different working fluids that included one wet fluid (HCFC-717), two isentropic fluids (HCFC-11 and HCFC-12) and two dry fluids (benzene and HCFC-113). These fluids have boiling temperatures in the range from 33.35°C to 79.85°C. The results showed that the highest system thermal efficiency was achieved when HCFC-11 and HCFC-113 working fluids were used [6]. Herath *et al.* studied a low-grade heat-source ORC for power generation and investigated seven working

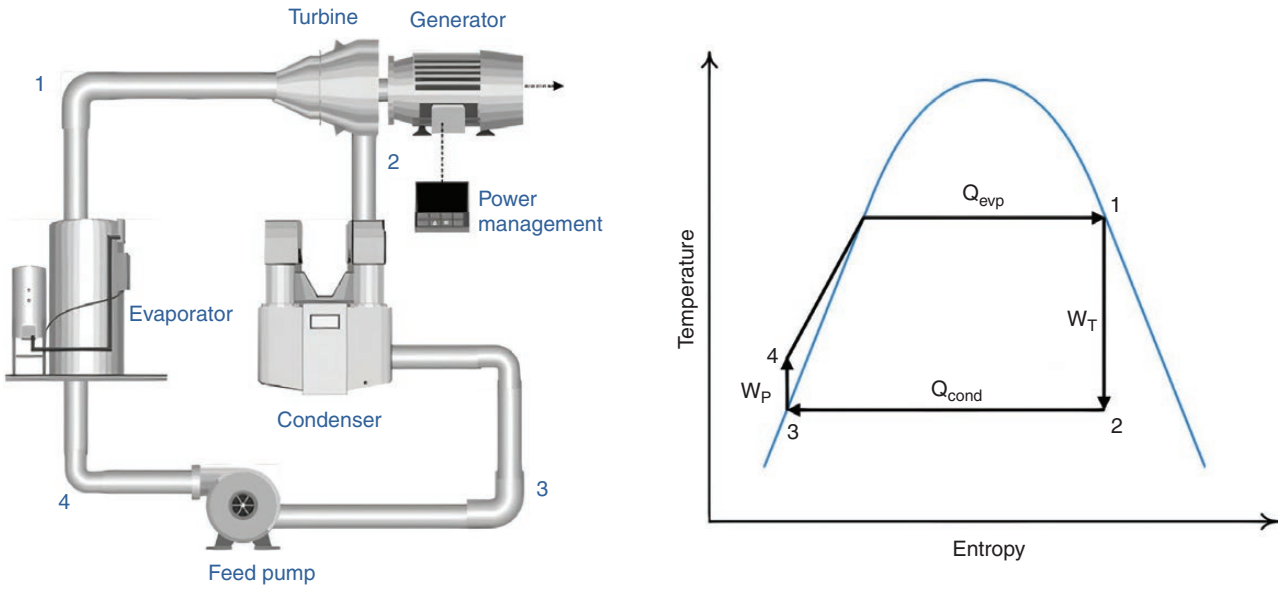

Fig. 1: Schematic diagram and T-s diagram of the ideal Rankine cycle

fluids: HCFC-134a, HCFC-245fa, methanol, ethanol, benzene, acetone and propane. Benzene showed a higher performance and had a thermal efficiency of between 14% and 19% using an evaporation temperature range from 100°C to 200°C compared to the other working fluids [7]. Yamamoto *et al.* investigated an ORC using a low-grade heat source. A ORC simulation model was designed for the system. Results demonstrated that HCFC-123 had higher performance than water with respect to turbine effective efficiency [8]. Thurairaja *et al.* conducted a working-fluid selection and performance evaluation of an ORC driven by a low-grade energy source. The results showed that cyclopentane for a temperature range of 50–100°C; butane, neopentane and R245fa for 100–150°C; ethanol, methanol and propanone for 150–200°C and water, m-Xylene and p-Xylene for 200–320°C were better working fluids for energy extraction [9]. Galloni *et al.* experimentally studied and analysed an ORC power system using R245fa as the working fluid. The system was investigated using both the thermodynamic and experimental set-up. The proposed source temperature range was 75–95°C. The maximum evaporation pressure of 10 bar was used and the condensation temperature range from 20°C to 30°C was set. The results showed that the output power of the system was 1.2 kW and the thermal efficiency was 9% [10].

The typical turbine isentropic efficiency range is 70–90%, as reported in the literature [11–13]. The ORC plants can be coupled to a wide range of design configurations of concentrating and non-concentrating solar collector types [14, 15]. Singh *et al.* reviewed the optimization, performance analysis and economic feasibility of different types of concentrating solar power technologies and suggested the linear Fresnel reflector (LFR) system as more economic for power units [16]. Ortega-Fernandez *et al.* investigated the thermal performance of a small-scale LFR–ORC power system. The plant was integrated with a packed-bed thermal-storage system consisting of magnetite ore, with a capacity of 16.6 MW, as the heat-storage medium. The solar field consisted of 16 400 m^2 of solar-panel area to operate a 1-MW ORC turbine system using a Delco Term Solar E 15 heat-transfer fluid (HTF) [17]. Zhu *et al.* investigated the thermal performance of the LFR model. The model is designed using a 6.6-m^2 collector field area for a latitude location having the direct normal irradiance of 851 W/m^2. The results showed that the maximum thermal efficiency of the LFR solar system was 64% for a transcal oil working fluid at a boiling point of 348°C [18]. Mokhtar *et al.* performed an experimental analysis of the LFR field for the solar heating system. The thermal efficiency of the system was >29% using a water working-fluid temperature of 74°C at Blida, Algeria [19]. Bellos *et al.* performed the solid work simulation of the LFR system, taking the solar-field aperture area and concentration ratio of 27 m^2 and 20.46, respectively. The yearly thermal efficiency was 18.5% using the optimum temperature value of 177°C of the working oil [20].

Xu *et al.* investigated the supercritical direct steam-generation ORC driven by the LFR. The analysis showed that the operating temperature range of the LFR power system was from 150°C to 350°C, and cyclohexane was the best working fluid with an efficiency of 19.65% [21]. Zhu *et al.* summarized the LFR technology and investigated the design concepts, technical challenges and performance of the technology in case of an intermediate temperature range [22]. Abbas *et al.* studied the different shapes of the secondary reflector of the LFR system to investigate their effect on the optical performance of the system. It was found that the LFR system efficiency using a secondary reflector was 23% higher as compared to that using a parabolic trough collector (PTC) [23]. Grena *et al.* presented an LFR model using molten nitrates as an HTF for high-temperature applications of 550°C. The thermal and optical

analyses of the model were performed using the simulation results. The study summarized the advantages and disadvantages of the system. The results showed that the molten-salt Fresnel system had a 15% lower value of efficiency than the traditional trough system [24]. Barbon *et al.* studied the effects of the longitudinal angles and latitude position on the performance of a small-scale LFR system [25]. Barbon *et al.* studied the effect of the transversal and longitudinal parameters on the thermal performance of the LFR system without a longitudinal movement. The analysis was performed using the design parameters of the LFR system including the receiver height, mirror length and mirror width, which had an influence on the thermal energy absorbed by a receiver tube [26]. Kincaid *et al.* studied the influence of the optical efficiency of the LFR field on the thermal efficiency of the power plant. The incidence-angle modifier coefficients and ray-tracing algorithm were used to determine the collector performance. The results showed that solar irradiance and latitude were important for plant-site selection [27]. Beltagy investigated the optical analysis of LFR for two absorber tubes. The model was based on Monte Carlo's racy tracing method. The annual optical efficiency of the system was found to be from 40.49% to 46.79% [28]. Bellos *et al.* studied the concentrating solar collector system at the latitude position of Athens, Greece. The monthly thermal performance of the LFR system was 49.66% in June [29]. Alain *et al.* determined the thermodynamic analysis and economic assessment of solar thermal power plants at a location in Cameroon (Africa). The results demonstrated an exergy efficiency value of 14.37% of the LFR system [30]. Ghodbane *et al.* studied the numerical simulation of the LFR system to generate the superheated steam for a power plant. The optical efficiency and thermal efficiency of the LFR system were observed at 53.7% and 37.5%, respectively, and the thermal losses were 5.84 W/m^2 °C [31].

The review of the previous published work shows that the majority of the work focussed on one part of the LFR–ORC system. In contrast, a few papers investigated both the LFR and ORC sections including optical and thermal aspects. Most of the published work was conducted using traditional refrigerants as working fluids in the ORC plant and usually oil or water as an HTF for the Fresnel system.

The present work deals with theoretical modelling and simulation design of the LFR model components using the solar-field dimension coupled with an ORC model. The selection of an appropriate working fluid is a difficult choice. NOVEC™ 649 is a good potential working fluid for the ORC that has a global-warming potential value of 1 and favourable safety properties causing low environmental impacts [32]. Because of the low critical temperature of NOVEC™ 649, it is applicable for low-temperature applications. The behaviour of the NOVEC™ 649 corresponds to the low-temperature thermal performance of the ORC plant and is the major contribution of this research. On the other hand, Therminol-62, as an HTF, has a wide range of temperature operation, high temperature of thermal stability and high heat-transfer coefficients, and delivers uniform heat even at low vapour pressure and is environmentally friendly as compared to water and other types of traditional HTFs [33]. Therminol-62 delivers process heat at low pressure and its high boiling point reduces the fluid-leakage and volatility problems associated with other fluids. Therminol-62 transfers the heat received from the solar irradiance into the working fluid NOVEC™ 649 of the ORC plant. Furthermore, such a system configuration along with the selected climatic conditions of Almatret, Spain, has not been investigated in the literature. The LFR is integrated with a two-tank storage system using an HTF and an energy-storage medium, extending the power-plant operation hours. Examining the annual performance of the LFR–ORC plant over different seasons with and without the thermal-storage system is a vital part of this study.

1 Methodology

Fig. 2 shows the schematic diagram of the LFR-driven ORC, which is linked with a thermal-storage system. The solar power ORC plant under investigation in this research work has three sections: the solar-field section, a thermal-storage section and a power-block section. The solar field consists of an LFR system. The thermal storage consists of a two-tank system (hot and cold). The thermal energy transfers between the solar field and thermal storage via a heat exchanger. The power block consists of a simple ORC. The power-plant performance will be evaluated based on the geographical and meteorological data of Almatret, Spain.

The solar organic Rankine-cycle (SORC) plant model was designed using the System Advisor Model (SAM) [34]. The dimension of the LFR was set and the actual weather data file was imported into the SAM at the Almatret latitude. The data file of the fluid properties of Therminol-62 was imported into the SAM fluid library. The ORC configuration was based on the working-fluid properties of the NOVEC™ 649. The power block does not determine the parasitic power using pressure consideration. The power block is characterized by the load-based coefficient and it is multiplied by the mass flow rate of the HTF. The thermal-storage system is connected to a heat exchanger. The thermal-storage heat losses are assumed to be constant and the fossil fuel required to meet the thermal-storage fluid target temperature is not calculated in this model. The movement of the Sun in the sky can cause a shadow on the LFR mirror patches. The LFR thermal losses because of the mirror surface shading effect are not considered at this stage.

1.1 The solar-field section (LFR field)

The incident rays are reflected from the surface of the Fresnel mirrors towards a 3-m-high fixed receiver tube. The Fresnel-field dimensions correspond to a specific size that produces an output thermal power of ~100 kW, depending on the solar radiation. The overall loop aperture area is assumed to be

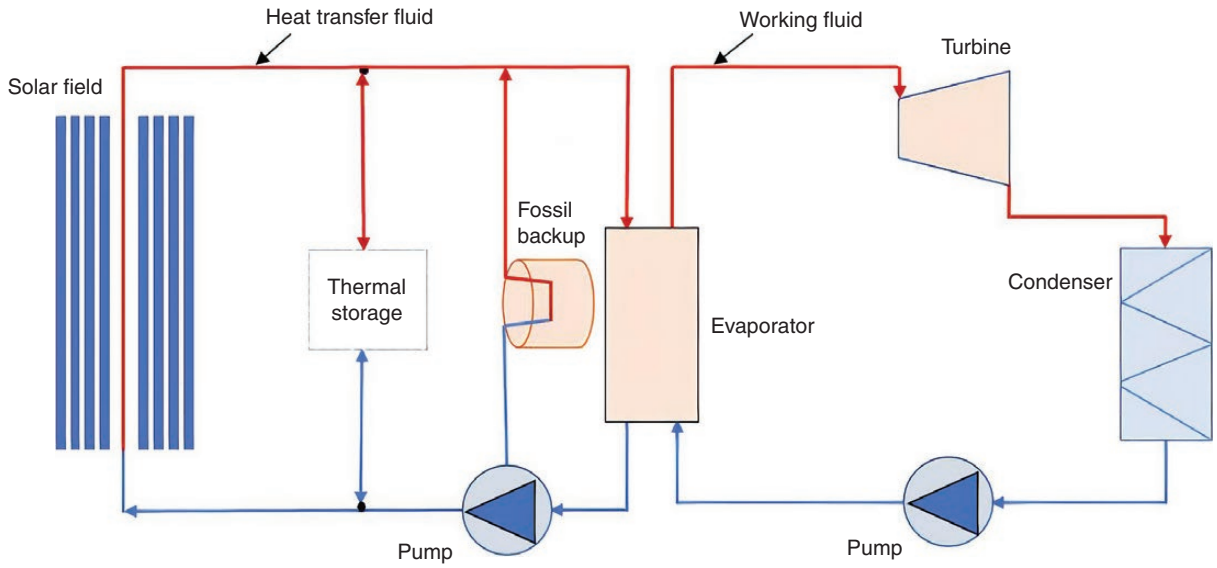

Fig. 2: Schematic diagram of an LFR-driven organic Rankine power cycle

214.38 m^2 and has a 0.3-m space between each module; the actual ground-covered area of the LFR solar-field system is 285.84 m^2. The LFR field has an arrangement of three parallel loops. Each loop configuration consists of modules that contain the series of Fresnel mirrors. There are nine modules in each loop. Each module area is 7.94 m^2 and calculated using the linear Fresnel mirror length and width. The loop area is 71.46 m^2 and is determined by adding the area of each module. Fig. 3 shows a diagram of the LFR field.

The HCEOI-12-type receiver tube is produced by Archimede Solar Energy [35] and is designed only for oil as an HTF. The maximum operating temperature of the fluid is 400°C inside the tube. The outer glass cover has an antireflective ceramic–metallic material coating, according to Ente per le Nuove Tecnologie l'Energia e l'Ambiente standards. The receiver tubes are equipped with secondary reflectors to maximize the concentration of solar thermal energy received by the surface of the primary mirror (see Fig. 4).

Tables 1–3 present some receiver characteristics, its core components, absorber tube and the glass envelope of the absorber tube. Tables 4 and 5 show the secondary reflector and Therminol-62, which is the receiver HTF.

In this study, the positions of the Fresnel mirrors change as a function of time (or Sun elevation and azimuth angles). The electronic unit determines the collector axis tilt as a function of the coordinates of the plant site, day of the year and current time. The performance of the LFR solar field will be investigated using the following parameters:

- the optical performance of the LFR field, which depends on the solar radiation available on the aperture and reaching the receiver;
- the thermal power output of the receiver tube that transfers to the HTF (Therminol-62);
- the thermal performance of the LFR field during the day-long operation hours and the thermal losses of the receiver tube.

The following assumptions are taken into consideration for the simplicity of the LFR field operation results:

- uniform temperature distribution of the receiver glass cover and steel pipe;
- steady-state and control volume conditions of the receiver tube and the temperature variation along the segment length is negligible;
- the fluid and solid properties are considered a function of the temperature, and the flow inside the receiver tube develops fully.

The value of the incident heat (Q_{inc}) was defined using the LFR system optical simulations and the LightTools software [37]. The Monte-Carlo ray-tracing method is used for analysis (see Fig. 5). In this optical systems modelling software, it is necessary to describe the geometry of the LFR field, as shown in Figs 6 and 7, and then, for a certain instance of time, to fix the position of the primary reflecting mirrors regarding the Sun's rays to reflect the operation of a Sun-tracking mechanism. Fig. 5 shows the mirrors in the initial arbitrary position. The simulation design model investigates the LFR performance of a specific day. The mathematical modelling is based on the heat-transfer equations to estimate the peak-hour thermal power produced and the thermal losses of the receiver tube.

Fig. 8 shows the heat-transfer mechanisms in a receiver tube. Q_{inc} is the incident heat of the focussed solar radiations and Q_{abs} is the heat absorbed by a steel pipe and then passed towards the HTF through the heat-conduction and heat-convection mechanisms (Q_{CDp} and Q_{CVi}). The convection heat transfer also occurred between the envelope outer surface of the glass envelope and the surrounding air (Q_{CVe}). There are heat losses into the environment through radiation (Q_{RDe}) and conduction in the glass cover (Q_{CDe}). Also, heat is lost through the radiative mechanism between the receiver glass cover and the secondary reflector surface (Q_t).

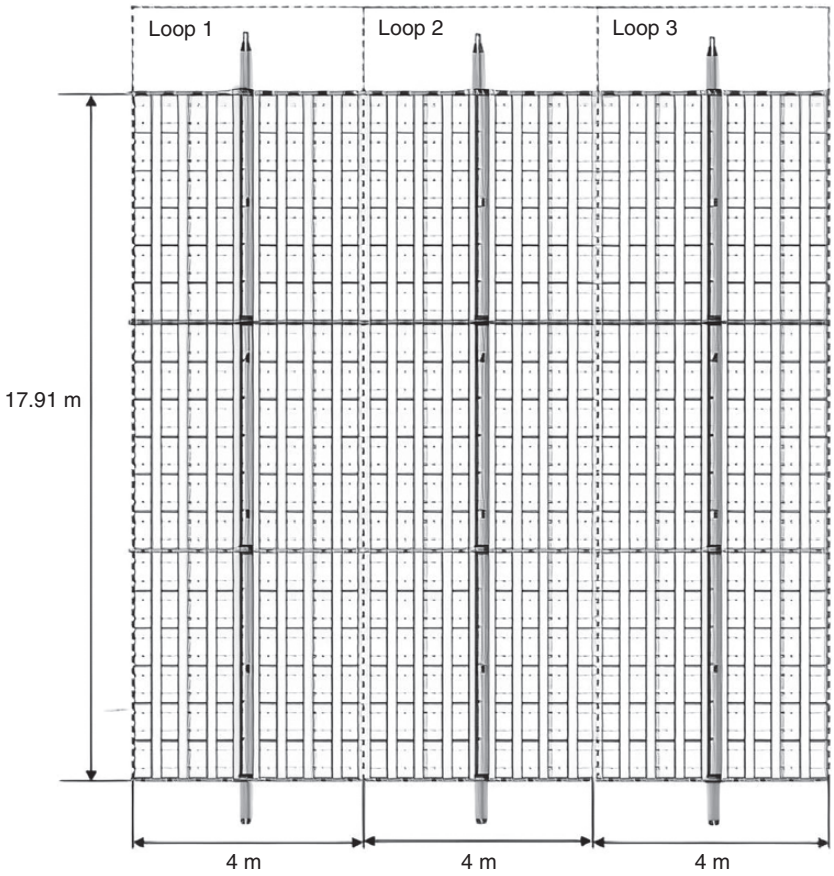

Fig. 3: Loop configuration of the LFR field

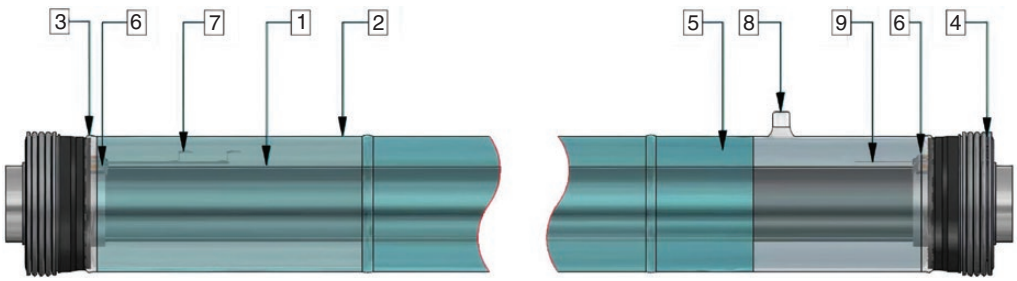

Fig. 4: Sketch of the receiver tube. Reprinted from [36], with permission from ASME.

(1) Stainless steel with the coating surface; (2) glass jacket with the antireflective coating surface; (3) glass-to-metal seals; (4) thermal-expansion getter pills; (5) vacuum annulus; (6) non-evaporable getter pills; (7) barium getter; (8) pump nipple; (9) serial number.

Table 1: Characteristics of the HCEOI-12 receiver [35]

Receiver weight	28 kg
Heat-transfer fluid	Therminol-62
Enclosure pressure	1 x 10^{-4} mbar
Lifetime	25 years
Stability of coating	The coating is stable in a vacuum at 600°C

The LFR field modelling in LightTools software produces information on the heat flux on the glass-cover surface from the primary mirrors and the secondary reflector, making it possible to find the incident heat rate rays on the

Table 2: Characteristics of the absorber tube of the HCEOI-12 receiver [35]

Material	Austenitic stainless-steel tube electric-welded longitudinally
Steel tube unit length	4060 mm
Steel tube thickness	2 mm
Steel tube outer diameter (D_{abs})	70 mm
Absorptance ($\alpha_{p,abs}$)	0.965
Emissivity ($\varepsilon_{p,abs}$)	0.085
Thermal conductivity ($K_{p,abs}$)	18.45 W/m.K

receiver tube. The heat energy gained by the HTF is determined in accordance with [26]:

$$Q_{gain} = \left(q_{flux-receiver,avg} A_a - Q_{loss}\right) \eta_{opt} \quad (1)$$

The value of the optical efficiency of the receiver is determined as a product of the glass envelope transmissivity (τ_g), absorber-tube absorptivity (α_p), mirror reflectivity (ρ_{mi}) and incidence-angle modifier (IAM):

$$\eta_{opt} = \tau_g \alpha_p \rho_{mi} IAM \quad (2)$$

The simplified thermal efficiency of the LFR system is the ratio of the amount of thermal energy absorbed by the HTF in the absorber tube to the product of the direct normal irradiance (DNI) value and the aperture area (A_{sc}) of the reflector (in m^2):

$$\eta = \frac{Q_{abs}}{A_{sc} DNI} \quad (3)$$

The total thermal losses are the sum of the convective heat losses to the environment, radiative heat losses from the receiver to the second reflector and radiative losses from the receiver to the environment:

$$Q_{loss} = Q_{CVe} + Q_r + Q_{RDe} \quad (4)$$

The convective heat transfer (Q_{CVe}) to the environment is calculated as:

$$Q_{CVe} = h_g A_{g,o} \left(T_{g,o} - T_o\right) \quad (5)$$

where h_g is the heat-transfer coefficient, the value of which depends on wind conditions; $A_{g,o}$ is the heat-transfer area from the glass cover (m^2); $T_{g,o}$ is the temperature of the glass (K); T_o is the ambient temperature (K).

The radiative heat transfer between the glass envelope and the secondary reflector is determined as:

$$Q_r = \frac{\sigma \left(T_{g,out}^4 - T_{sr,in}^4\right)}{\left(\frac{1-\varepsilon_g}{A_{g,out}\varepsilon_g} + \frac{2}{A_{g,out}} + \frac{1-\varepsilon_{sr}}{A_{sr,in}\varepsilon_{sr}}\right)} \quad (6)$$

The radiative heat transfer between the outer surface of the glass envelope and the environment is defined as:

$$Q_{RDe} = \frac{\sigma \left(T_{g,out}^4 - T_{env}^4\right)}{\left(\frac{1-\varepsilon_g}{A_{g,out}\varepsilon_g} + \frac{2}{A_{g,out}}\right)} \quad (7)$$

where σ is the Stephan-Boltzmann constant, equal to 5.67 x 10^{-8} $W/m^2.K^4$.

The IAM coefficients are calculated as the polynomial functions. In the case of the transverse plane, the equation is:

Table 3: Characteristics of the glass envelope of the HCEOI-12 receiver [35]

Material	Borosilicate
Glass-tube length	3900 mm
Glass-tube thickness	3 mm
Glass-tube outer diameter ($D_{g,in}$)	125 mm
Glass-tube inner diameter ($D_{g,out}$)	121 mm
Glass-cover absorptance (α_g)	0.02
Glass-cover emissivity (ε_g)	0.86
Glass-cover transmittance (τ_g)	0.965
Glass-cover thermal conductivity (K_g)	1.4 W/m.K

Table 4: Characteristics of the secondary reflector of the HCEOI-12 receiver [35]

Material	Coated aluminium
Opening width (w_{ref})	0.15 m
Reflectivity (ρ_{sr})	0.90
Emissivity (ε_{sr})	0.105
Absorptance (α_{sr})	0.03

Table 5: Properties of Therminol-62 [33]

Composition	Isopropyl biphenyl mixture
Appearance	Water-white liquid
Maximum bulk temperature	325°C
Normal boiling point	333°C
Minimum use temperature	–23°C
Heat of vapourization	263.9 kJ/kg
Liquid density (at 25°C)	951.1 kg/m^3
Pseudocritical temperature	487°C
Pseudocritical pressure	15 bar
Pseudocritical density	269.4 kg/m^3

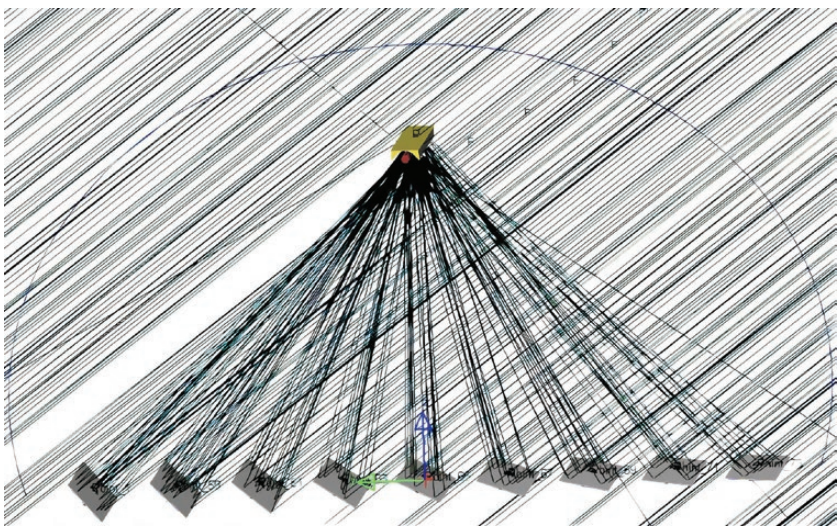

Fig. 5: Modelling of the LFR module using the LightTools software

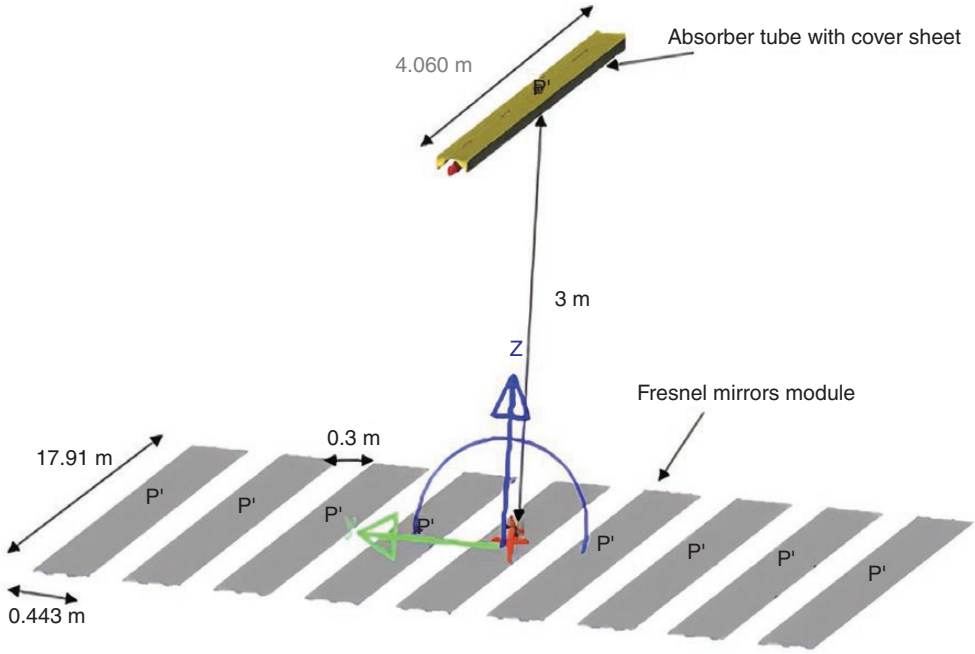

Fig. 6: The design of the LFR module for the LightTools simulations

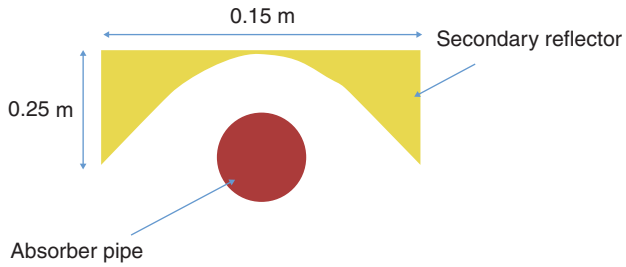

Fig. 7: The secondary reflector with the absorber tube for the LightTools simulations

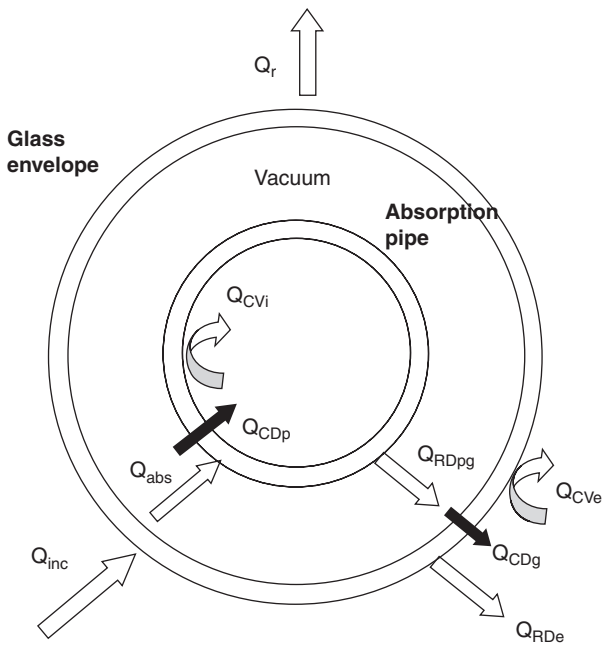

Fig. 8: Heat-transfer mechanisms in the receiver tube. Reprinted from [38], with permission from Elsevier.

Table 6: Transversal and longitudinal IAM coefficients [26]

Component	C_o	C_1	C_2	C_3	C_4
Transversal IAM coefficients	1.007	2.256^{-09}	-4.479^{-07}	2.802^{-05}	-7.134^{-04}
Longitudinal IAM coefficients	1.000	9.996^{-10}	-1.869^{-07}	1.274^{-05}	-4.927^{-04}

$$IAM_T = C_o + C_1\phi_T + C_2\phi_T^2 + C_3\phi_T^3 + C_4\phi_T^4 \quad (8)$$

where ϕ_T indicates the transversal incidence angle (in degrees).

In the case of the longitudinal plane, the equation is:

$$IAM_L = C_o + C_1\phi_L + C_2\phi_L^2 + C_3\phi_L^3 + C_4\phi_L^4 \quad (9)$$

where ϕ_L indicates the longitudinal angle.

Table 6 shows the values of the constant coefficients for the above polynomial functions.

The total IAM coefficient is determined as:

$$IAM = IAM_T \times IAM_L \quad (10)$$

1.2 The thermal-storage section

Fig. 9 shows the two-tank thermal-storage system. A portion of the high-temperature Therminol-62 ($T_{1,in}$) transfers the thermal energy to the lower-temperature Therminol-62 via a heat exchanger during the peak hour of solar irradiance. There is a counterflow mechanism between these fluids. The Therminol-62 in the cold tank ($T_{2,out}$) circulates to the hot-tank system using a pump. This process is known as the charging of the thermal-storage system. The hot-tank discharging process takes place using a circulation pump to extend the power-plant operation hours. The hot-fluid temperatures of the heat exchanger ($T_{1,in}$ and

$T_{1,out}$) are the working-fluid temperatures at the outlet and inlet of the solar collector, respectively. The set temperatures of the cold tank ($T_{2,in}$) and target temperature ($T_{2,out}$) are assumed to be 40°C and 173.5°C, respectively. The fossil-fuel back-up is also integrated with the power system to meet the thermal-storage system target temperature. The thermal characteristics of the hot and cold fluids are listed in Table 7.

The thermal capacity (C) of the storage-tank system is the product of the total load hours with a ratio of the reference output electrical power under design conditions (W_{des}) and the power-cycle conversion efficiency (η_{des}). The W_{des} and η_{des} values are assumed to 20 kW and 14%, respectively, for four load hours (T_{load}) of the thermal-storage system:

$$C = \frac{w_{des}}{\eta_{des}} \times T_{load} \tag{11}$$

The Therminol-62 fluid is used in the thermal-storage system. There are two types of thermal-storage systems. If the heat-transfer solar-field fluid and storage fluid are different, the system is indirect storage. In this case, the heat exchanger derates (μ_h) has a value of <1. The direct thermal-storage system used in the current model is based on the hot and cold tanks. The solar field and storage system have the same type of fluid, namely Therminol-62. The cold-tank

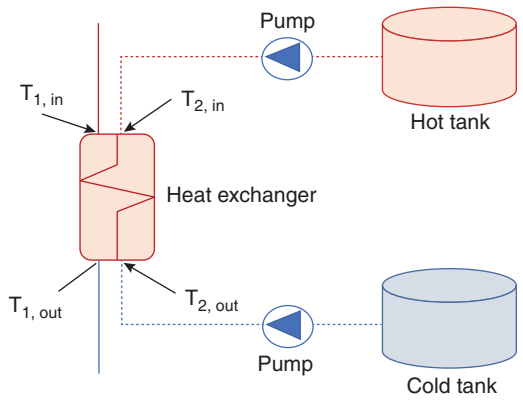

Fig. 9: Thermal-storage system of the plant

Table 7: Thermal characteristics of the hot and cold fluids of the heat exchanger

Parameters	Value
Heat-exchanger hot-fluid inlet temperature ($T_{1,in}$)	280°C
Heat-exchanger cold-fluid outlet temperature ($T_{1,out}$)	67°C
Heat-exchanger cold-fluid inlet temperature ($T_{2,in}$)	40°C
Heat-exchanger cold-fluid outlet temperature ($T_{2,out}$)	173.5°C
Specific heat of hot fluid ($C_{p,h}$)	2.44 kJ/kg.K
Specific heat of cold fluid ($C_{p,c}$)	1.99 kJ/kg.K
Mass flow rate of hot fluid ($\dot{m}_h$)	0.205 kg/s
Mass flow rate of hot fluid ($\dot{m}_c$)	0.300 kg/s

fluid transfers from the cold tank to the hot tank via a heat exchanger and absorbs heat energy from the solar-field fluid known as the HTF. It has a density (ρ_{htf}) of 830 kg/m³ and specific heat (C_{htf}) of 2.440 kJ/kg.K. The derate factor of the HTF is considered as 1 for a direct system. The storage volume of the fluid tanks is calculated by using the expression:

$$V_T = \frac{C \times 3600,000}{\rho_{htf} \times C_{htf} \times \mu_h \times 1000 \times (T_{s,out} - T_{s,in})} \tag{12}$$

The height (H) of the storage tank is assuming to be 5 m. The storage system has one pair of tanks (N_p), which consists of a cold tank and a hot tank. The diameter (D) (in m) of the tank is calculated using the following expression:

$$D = 2\sqrt{\frac{V_T}{H \times \pi \times N_P}} \tag{13}$$

The heat-loss factor of the storage-tank system depends upon the height (H) (in m), diameter (D), number of pairs (N_p), average fluid temperature (T_{avg}) and loss coefficient of the tank (C_{loss}). The hot and cold fluids at the inlet of the tank are at 280°C and 40°C, respectively. The average fluid temperature is calculated using the expression:

$$T_{avg} = \frac{T_{h,tank} + T_{c,tank}}{2} \tag{14}$$

The loss coefficient (C_{loss}) of the tank is assumed to be 0.2 W/m².K. The amount of heat energy lost (H_{loss}) by a tank storage system is calculated using the following expression:

$$H_{loss} = \left(H \times \pi \times D + \pi \times \left(\frac{D}{2}\right)^2\right) N_P \times (T_{avg} - 20) \times C_{loss} \tag{15}$$

The effectiveness (ϵ) of the intermediate counterflow heat exchanger depends on the ratio of the temperature difference of the heat-transfer and working fluids and the specific heat-capacity ratio (c) of these fluids:

$$\epsilon = \frac{C_{p,h}\,(T_{sc2} - T_{sc1})}{C_{p,c}\,(T_{sc2} - T_{htf1})} \tag{16}$$

The number of transfer units (NTU) of the counterflow heat exchanger depends on the specific heat-capacity ratio of the hot- and cold-fluid streams and the effectiveness of the heat exchanger:

$$NTU = \frac{1}{C_r - 1} \ln \frac{\epsilon - 1}{\epsilon C_r - 1} \tag{17}$$

1.3 The power-block section

NOVEC™ 649 belongs to the ketone family and is called ethyl isopropyl ketone. NOVEC™ 649 has a wide range of applications in various ORCs. It has excellent thermal stability and it is non-corrosive for ORC components. It is environmentally friendly, has low toxicity and is non-flammable. NOVEC™ 649 has a global warming potential value (100-year integration horizon time value) of 1 and an ODP (ozone depletion potential) value of zero [32]. Table 8 shows the properties of NOVEC™ 649 as the working fluid.

Table 8: Properties of NOVEC™ 649 [39]

Chemical formula	$C_6H_{12}O$
Molecular weight	0.31604 kg/mol
Boiling point at 1 a.t.m.	49°C
Freezing point	<–100°C
Critical temperature	169°C
Critical pressure	18.7 bar
Kinematic viscosity	0.42 CST
Specific heat	1.103 kJ/kg.K
Thermal conductivity	0.059 W/m.K

Table 9: Theoretical estimations of the ORC plant parameters

Parameter	Value
Mass flow rate	0.2 kg/s
Evaporation pressure	15 bar
Condensation pressure	1 bar
Isentropic efficiency of the turbine	75%

Table 10: Performance equations of the ORC plant system

Description	Equation	
Evaporation heat input	$\frac{Q_{evp}}{\dot{m}_{wf}} = (h_2 - h_1)$	(18)
Turbine expansion work	$\frac{W_T}{\dot{m}_{wf}} = (h_3 - h_2)$	(19)
Condensation heat rejection	$\frac{Q_{cond}}{\dot{m}_{wf}} = (h_4 - h_3)$	(20)
Pump work input	$\frac{W_P}{\dot{m}_{wf}} = (h_4 - h_1)$	(21)

Table 9 shows the operating condition of the ORC plant. The Rankine-cycle operating parameters are based on the parametric analysis of the design variables to produce mechanical power of ≤7.2 kW and correspond to the cycle thermodynamic performance of the individual components. The turbine output pressure has the same value as the condensation pressure.

The following are the set of assumptions considered in this study to investigate the thermodynamic performance of the ORC system:

- Each component in the cycle is considered as a control volume and the model operation is described by using the steady-state steady-flow condition.
- The kinetic- and potential-energy changes are assumed to be zero and the heat-loss effects are negligible.
- The isentropic efficiency of both the turbine and the pump is 75%.

Table 10 shows the set of thermodynamic equations used to evaluate the thermal performance of the ORC plant, which depends on the enthalpy change (h).

The isentropic turbine efficiency is the ratio between the real turbine work output to the turbine work output under ideal conditions. It can be expressed in terms of the enthalpy change during the expansion process as:

$$\eta_{T,is} = \frac{h_{in} - h_{out}}{h_{in} - h_{ideal}} \quad (22)$$

Fig. 10 shows a schematic of the developed ORC model using the Thermolib simulation tool, having four components including the evaporator, turbine, condenser and pump. This tool has been proved as being powerful for the modelling of thermodynamic systems [40, 41]. NOVEC™ 649 is a working fluid that circulates within the system components in a cyclic process under a steady-state process. In the evaporator or condenser, the working fluid is heated or condensed at its saturation temperature of a given value of the working pressure. The turbine reduces the pressure of the incoming fluid to a target value and calculates the thermodynamic state of the outgoing fluid and the mechanical power produced at a given value of the isentropic efficiency. The pump elevates the condenser outlet pressure of the working fluid to the evaporator pressure. The enthalpy difference using a 0.2-kg/s mass flow rate of the NOVEC™ 649 working fluid determines the performance of the ORC components.

2 Results and discussion

Figs 11 and 12 show the variations of the Sun elevation in the sky and its azimuth angle during the day in Almatret on 7 July. The elevation angle of the Sun has a higher value after the mid hour of the day and the azimuth angle value is 177° at 13:00. These angles correspond to the higher thermal performance of the LFR reflector. The elevation angle approaches zero at 19:00 with the highest value of the azimuth angle.

Fig. 13 shows graphics of the variation in the calculated global horizontal irradiance (GHI), and DNI and diffuse horizontal irradiance (DHI) in Almatret in July. The GHI is the combination of the DNI using the incidence angle of the beam and the DHI. This information was used as one of the input parameters in the LightTools modelling of the LFR system. The maximum value of the GHI is 900 W/m^2 and it is achieved at 13:00.

Fig. 14 shows the ray-tracing simulation results to determine the values of the longitudinal and transverse components of the IAM for the LFR system. The heat gained by the HTF increases with a higher value of the IAM. The incidence angle relates to the thermal performance of the LFR system. The higher value of the incidence angle causes the reduction in the IAM coefficients.

The thermal loss (Q_{loss}) of the solar collector is calculated using Equation (4) and has a value of 7.872 kW during the peak time of the day at 1:00 p.m. The convective heat transfer (Q_{CVe}) occurs between the outer surface of the glass envelope to the vacuum. It is the space between the secondary reflector and the glass envelope considering convective heat-transfer losses. The heat-transfer coefficient value is considered to be 100 W/m^2.K in the case of medium air. The convective heat transfer (Q_{CVe}) has a value of 7.66 kW. The radiant heat-transfer losses (Q_r) occur between the glass envelope and the secondary reflector. In the outer glass envelope and secondary reflector, the inner

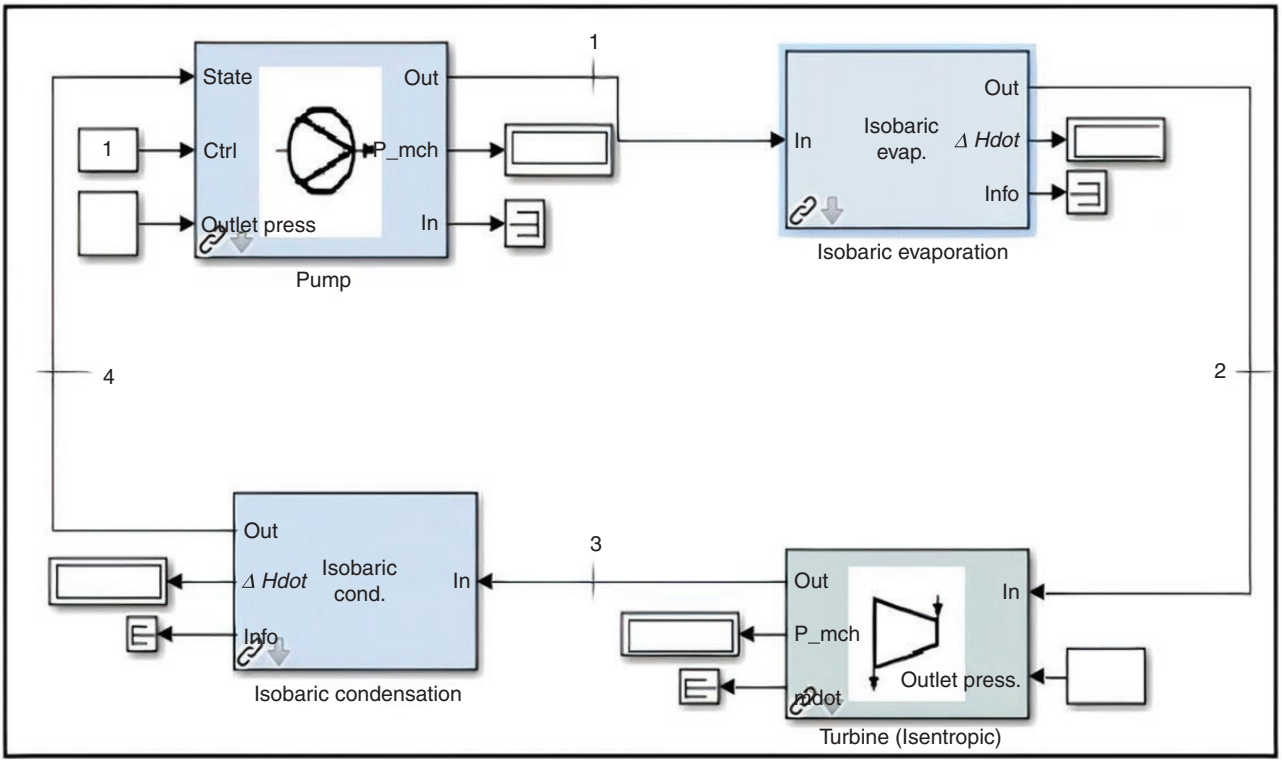

Fig. 10: The schematic of the ORC in the Thermolib simulation model

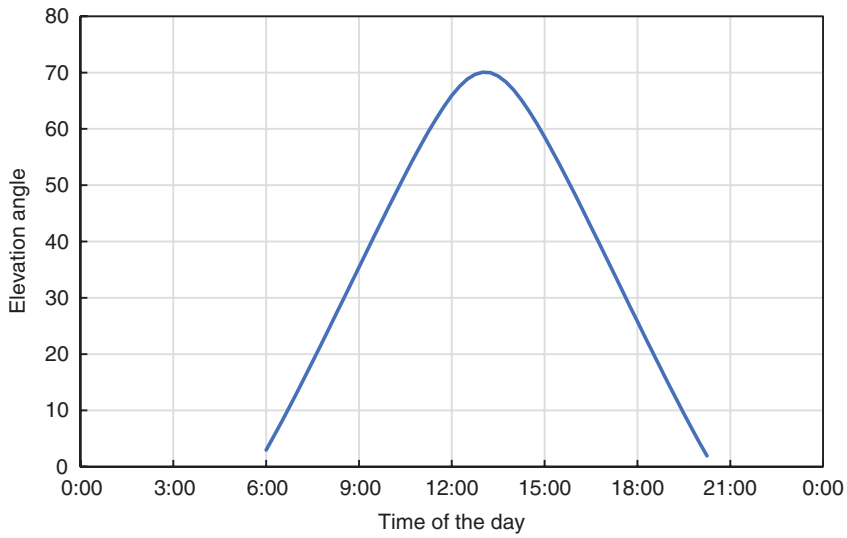

Fig. 11: Sun elevation angle during the day of 7 July in Almatret

temperatures are 130°C and 80°C, respectively. The radiant heat losses are 9.783 W. There are radiant heat-transfer losses (Q_{RDe}) between the outer surface of the glass envelope and the environment. The outside temperature of the environment is considered to be 25°C. The radiant heat-transfer loss is 11.450 W. These results correspond to Fig. 15, which shows the calculated total magnitude of the heat losses from the receiver to the ambient and the secondary reflector due to convection and radiative heat-loss mechanisms of a day using the simulation run of the LFR model in LightTools.

Finally, Fig. 16 presents the determination of the variation in the heat rate absorbed by the HTF after taking into account the optical efficiency of the receiver and heat losses to the environment. The maximum thermal power transferred to the HTF (Therminol-62) is ~108 kW during the day at the peak hour. The results are calculated using the dimension of the LFR field as discussed above, weather

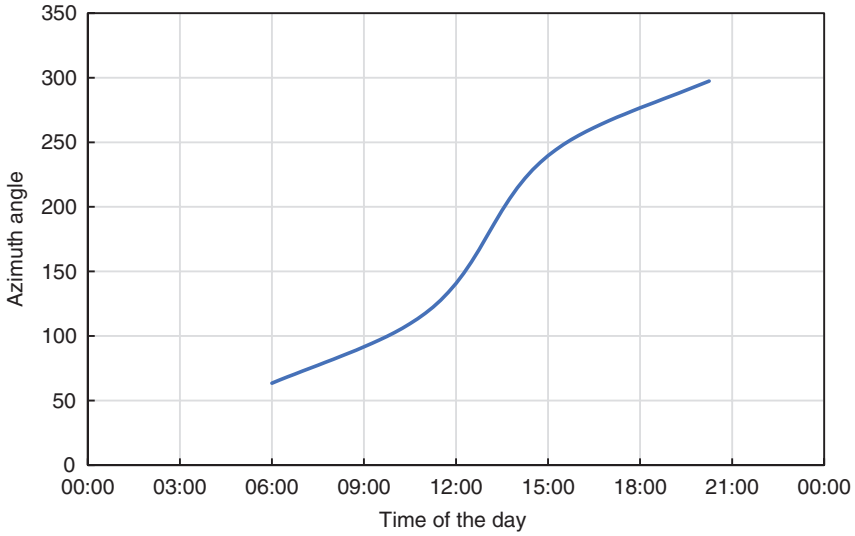

Fig. 12: Sun azimuth angle variation during the day of 7 July in Almatret

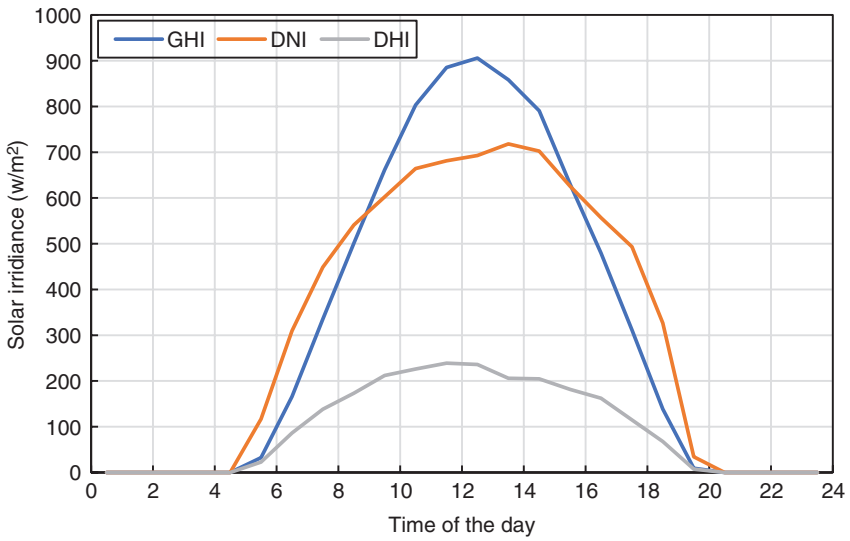

Fig. 13: GHI, DNI and DHI variations in July

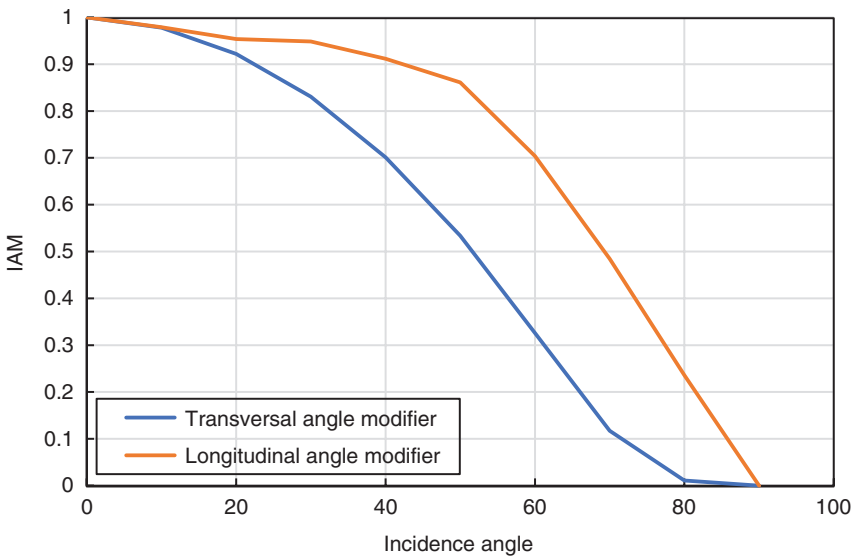

Fig. 14: IAM coefficients at different values of incidence angle

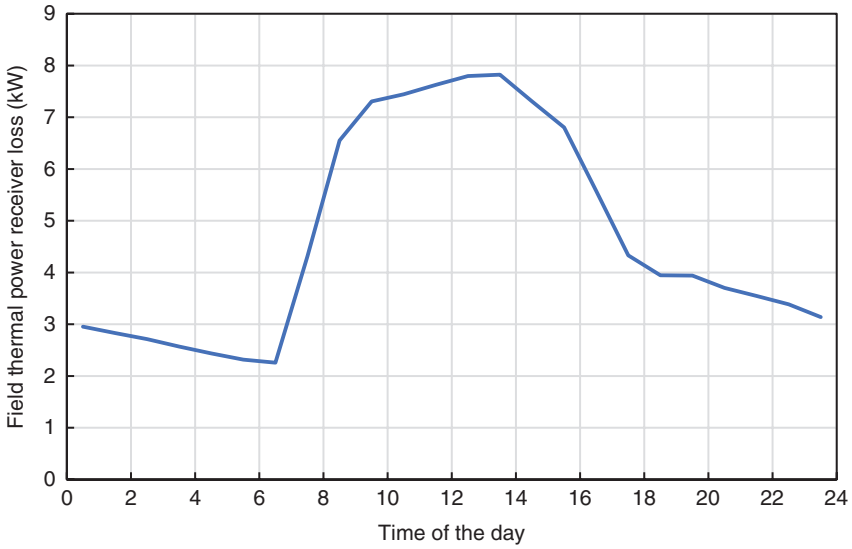

Fig. 15: Variation in the thermal losses from the receiver during the day

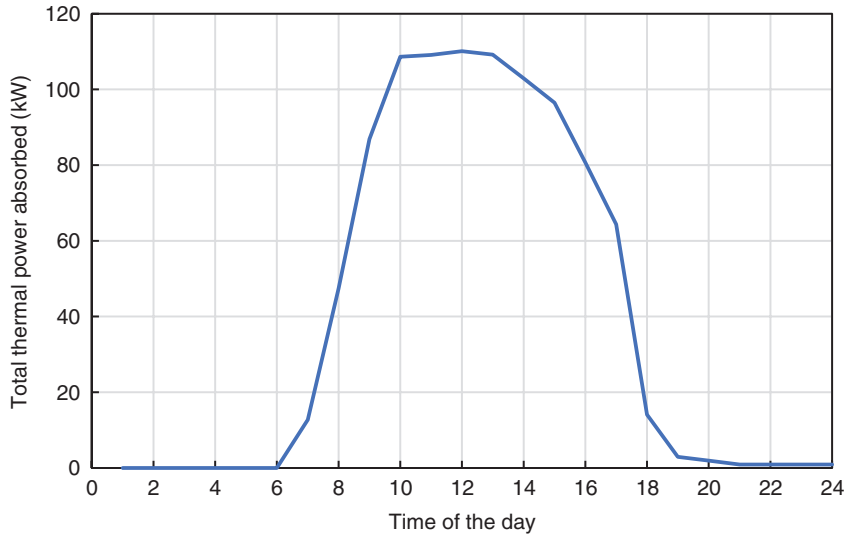

Fig. 16: Variation in the amount of the thermal power absorbed by the HTF during the day

data of the Almatret latitude and Therminol-62 HTF. The thermal performance of the LFR depends on the solar irradiance during the day and this information can then be used in the calculation of the other main parts of the SORC.

Fig. 17 shows both the optical efficiency and the thermal efficiency of the solar field in the month of July. The optical efficiency of the LFR is the fraction of the solar radiation incident on the glass cover and transfers to the HTF of the absorber tube. The values of these efficiencies change with the position of the Sun during the day. The higher value of the solar incidence angle creates higher-end collector losses and reduces the efficiency of the plant. This is attributed to the variations in the values of both the DNI and the IAM. Such variations in the optical and thermal efficiencies influence the performance of the SORC system. As shown in the figure, they have their maximum values during the daily peak hour of ~60.4% and ~42.7%, respectively.

In order to validate the developed model, a comparison between the simulation model results of the ORC system and the thermodynamic data from the NIST Reference Fluid Thermodynamic and Transport Properties Database was performed as shown in Table 11. This comparison was conducted on 7 July at 1:00 p.m., when the highest thermal-energy level is supplied to the ORC (46.432 kW) and the turbine power is 7.296 kW. The mass flow rate of NOVEC™ 649 (m_{wf}) is 0.2 kg/s. The thermal efficiency of the ORC is 15.6%. The thermodynamic performance of the ORC model is calculated using the equations illustrated in Table 10. The thermodynamic data are obtained during the similar peak-hour operating conditions of the simulation model of the ORC. The enthalpy values of the NOVEC™ 649 are determined using REFPROP version 10. As shown in Table 11, the values calculated using the simulation model and those obtained from REFPROP are in very good agreement. The maximum relative deviation is <10%.

In this mode of operation, the ORC generates an output power value of >7 kW between about 9:30 and 16:30, as shown in Fig. 18. Due to the variation in DNI during the day, there is a sharp decrease in the power generated after about 17:30, reaching a value of only 3.14 kW at 19:30. In addition, during the period between 9:30 and 16:30, the solar field produces higher thermal energy than is required for the ORC to generate the maximum power (see Fig. 16). Therefore, a comparable amount of such excess heat energy is wasted during the day. However, this surplus can be recovered if a thermal-energy-storage system is integrated with the SORC as illustrated in Fig. 2. Fig. 19 shows the variation in the generated power of the SORC with a thermal-storage system. It can been seen that the scenario of the implementation of a thermal-storage system offers a chance to reuse the accumulated thermal energy to run

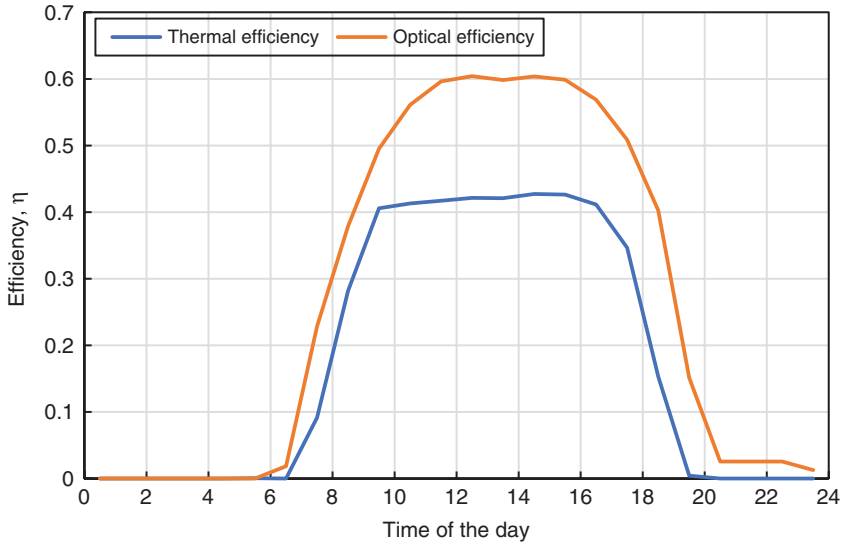

Fig. 17: Optical and thermal efficiency of the LFR during the day

Table 11: Comparison of the simulation model results of the ORC with thermodynamics results

Parameter	Simulation model results	Data from REFPROP	Percentage deviation
Evaporation heat input at15 bar and 450 K (kW)	46.432	42.432	9.43
Turbine outlet power at 1 bar and 400 K (kW)	7.296	6.856	6.42
Condensation heat rejection at 1 bar and 281 K (kW)	22.138	22.146	-0.04
Pump input power at 15 bar and 280 K (kW)	0.32	0.3128	2.30

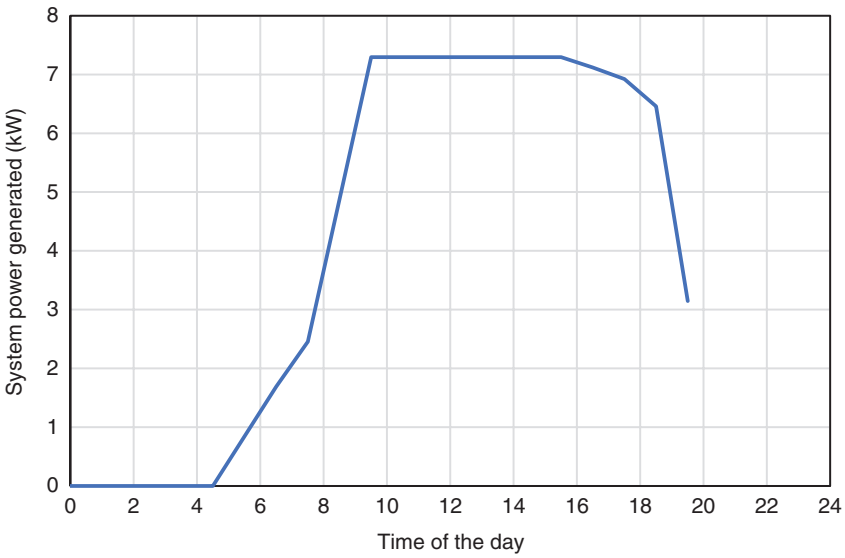

Fig. 18: ORC power generation during a day in July without the thermal-storage system

the ORC from about 19:30 to 23:30. As shown in Figs 18 and 19, it is worth mentioning that the SORC with the thermal-storage system extends the system operation by ~4 hours for the selected day. However, the maximum power generated remains the same in both cases. This is because the input heat source to the SORC is the same.

The thermal capacity of the storage system is 571.42 kW. The storage volume (V_T) of the fluid tanks is 4.23 m^3. The tank diameter (D) is 1.03 m and the average fluid temperature is 173.5°C in the hot tank. The amount of heat energy lost (H_{loss}) by a tank storage system is 521.691 W. The capacitance rate (C) is the ratio of the minimum and maximum specific heats of the fluid. It has a value of 0.80. The effectiveness (ε) of the heat exchanger is 0.746. The *NTU* of the counterflow heat exchanger is 2.13.

The simulations were repeated for every month in a year, using statistical data on the average solar irradiation for Almatret. Fig. 20 shows the annual performance of the SORC with and without a thermal-storage system. It can be seen that the ORC plant has a significant increase in the thermal performance from May to August, producing the highest monthly energy output in July. The total produced energy values in July with and without the thermal-storage system are ~2160 and ~1487 kWh, respectively, which corresponds to the maximum values of the GHI and sunlight duration. During the months of May to August, integrating the thermal-storage system offers an average percentage increase in the monthly generated energy of between 40% and 45%. The lowest amount of plant monthly energy is produced in January with values of 147 and 139 kWh, with and without the thermal-storage system, respectively. In this month, the thermal storage is not engaged with the plant operation very much, which adds <6% of the total energy generated.

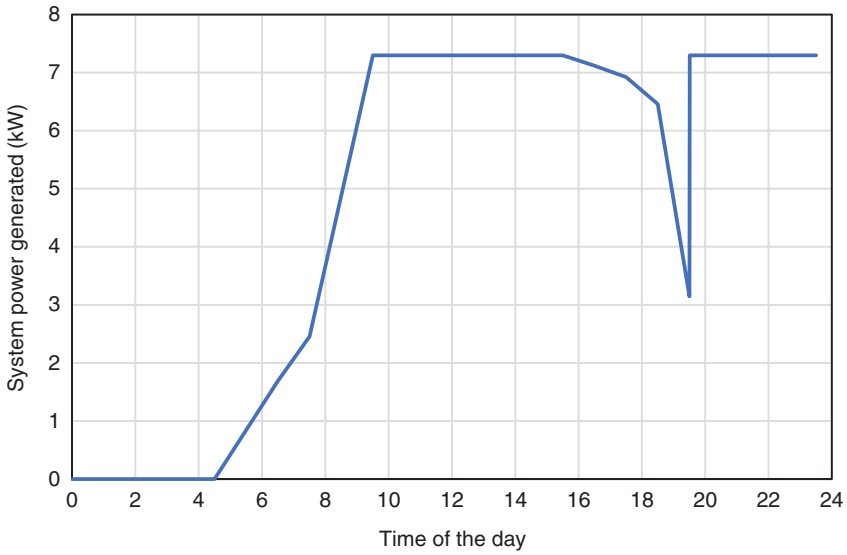

Fig. 19: ORC power generation during a day in July with the thermal-storage system

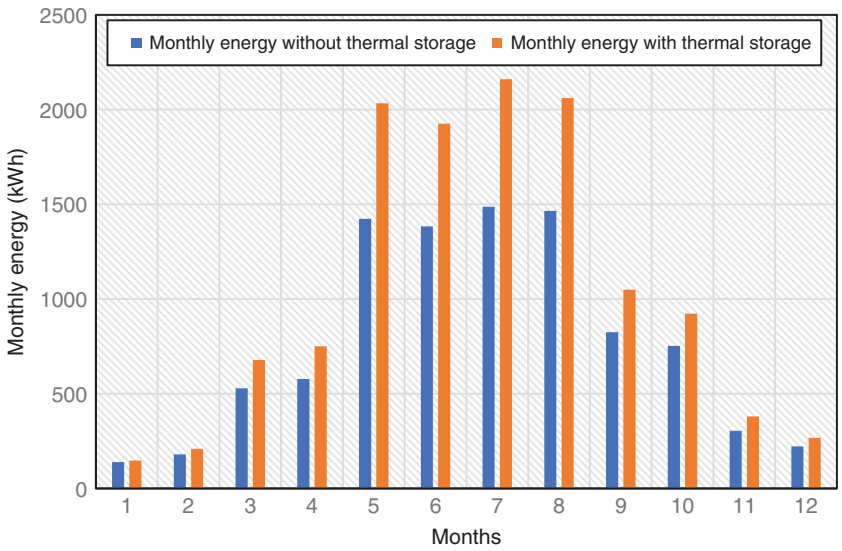

Fig. 20: Annual energy generation by the SORC with and without the thermal-storage system

3 Conclusions

The theoretical model for describing the LFR–ORC integrated with a two-tank thermal-storage system was developed. The thermal performance of the LFR receiver using the Therminol-62 HTF was investigated. The LFR model was based on applying LightTools software for optical modelling of the solar field based on the Monte-Carlo ray-tracing method. For the given configuration of the solar field of certain dimensions, the software allowed the calculation of the heat flux on the receiver surface due to solar energy concentration by the primary mirrors and secondary reflector of the solar field. The data on the heat fluxes were then used to determine the thermal state of parts of the receiver, making it possible to estimate the heat losses in the system and determine the heat absorbed by the HTF of the solar field.

The performance of the LFR–ORC with the solar field and thermal-storage system was modelled. The working fluid used in the ORC was NOVEC™ 649. The thermal storage was charged only when the solar field generated more thermal energy than was necessary for the ORC operation at its maximum power output mode using Therminol-62 as the HTF. The single-axis tracking system of the LFR utilized the maximum solar irradiance during a day. The Therminol-62 had good results in the LFR solar field to drive the ORC power unit. The thermodynamic and simulation analysis showed that the LFR field aperture area was 214.38 m^2 with a receiver tube at 3 m high above the Fresnel mirror surface. The maximum output monthly power produced was 2160 kWh in July and 7.2 kW output power during the peak hour of 7 July. The two-tank system stored the thermal energy via a heat exchanger using the Therminol-62 fluid and increased the ORC plant operation by 4 hours beyond sunset. Moreover, the use of a thermal-storage system increased the total energy produced monthly by ≥40% during the months between May and August. In the winter months, the thermal performance of the SORC was low and the thermal-storage system did not engage with the system.

Acknowledgements

The authors are thankful to the Graduate School at Northumbria University for providing the financial support to purchase the simulation tools.

Conflict of interest statement

None declared.

References

[1] Rahbar K, Mahmoud S, Al-Dadah RK. Mean-line modelling and CFD analysis of a miniature radial turbine for distributed power generation systems. *International Journal of Low-Carbon Technologies*, 2014, 11:157–168.

[2] Tartiere T, Astolfi MA. World overview of the organic Rankine cycle market. *Energy Procedia*, 2017, 129:2–9.

[3] Ganjehsarabi H, Asker M, Seyhan AK. Energy and exergy analyses of a solar assisted combined power and cooling cycle. In: *2016 IEEE International Conference on Renewable Energy Research and Applications (ICRERA)*, IEEE, Birmingham, UK, 20 November 2016, 1141–1145.

[4] Wang S, Liu C, Li Q, *et al*. Selection principle of working fluid for organic Rankine cycle based on environmental benefits and economic performance. *Applied Thermal Engineering*, 2020, 178:115598.

[5] Tchanche BF, Papadakis G, Lambrinos G, *et al*. Fluid selection for a low-temperature solar organic Rankine cycle. *Applied Thermal Engineering*, 2009, 29:2468–2476.

[6] Santiago RE, Joao AC, Antonio PB. Effect of working fluids on organic Rankine cycle for the recovery of low-grade waste heat. In: *Proceedings of the 12th Latin American Congress on Electricity Generation and Transmission—CLAGTEE*, Mar del Plata, Argentina, 12–17 November 2017, 1–6.

[7] Herath HMDP, Wijewardane MA, Ranasinghe RACP, *et al*. Working fluid selection of organic Rankine cycles. *Energy Reports*, 2020, 6:680–686.

[8] Yamamoto T, Furuhata T, Arai N, *et al*. Design and testing of the organic Rankine cycle. *Energy*, 2001, 26:239–251.

[9] Thurairaja K, Wijewardane A, Jayasekara S, *et al*. Working fluid selection and performance evaluation of ORC. *Energy Procedia*, 2019, 156:244–248.

[10] Galloni E, Fontana G, Staccone S. Design and experimental analysis of a mini ORC (organic Rankine cycle) power plant based on R245fa working fluid. *Energy*, 2015, 90:768–775.

[11] Bianchi M, De Pascale A. Bottoming cycles for electric energy generation: parametric investigation of available and innovative solutions for the exploitation of low and medium temperature heat sources. *Applied Energy*, 2011, 88:1500–1509.

[12] Gu Z, Sato H. Performance of supercritical cycles for geothermal binary design. *Energy Conversion and Management*, 2002, 43:961–971.

[13] Hossin K, Mahkamov K, Belgasim B. Thermodynamic analysis and sizing of a small scale solar thermal power system based on organic Rankine cycle. *Journal of Sustainable Development of Energy, Water and Environment Systems*, 2020, 8:493–506

[14] Petrollese M, Cocco D. Robust optimization for the preliminary design of solar organic Rankine cycle (ORC) systems. *Energy Conversion and Management*, 2019, 184:338–349.

[15] Casartelli D, Binotti M, Silva P, *et al*. Power block off-design control strategies for indirect solar ORC cycles. *Energy Procedia*, 2015, 69:1220–1230.

[16] Singh H, Singh A, Mishra RS, Pal A. A current review on linear Fresnel reflector technology and its applications in power plants. In: Kumar A, Pal A, Kachhwaha SS, Jain PK (eds). *Recent Advances in Mechanical Engineering. Lecture Notes in Mechanical Engineering*. Singapore: Springer, 2021, 431–440.

[17] Ortega-Fernandez I, Hernández A, Wang Y, *et al*. Performance assessment of an oil-based packed bed thermal energy storage unit in a demonstration concentrated solar power plant. *Energy*, 2021, 217:119–378.

[18] Zhu Y, Shi J, Li Y, *et al*. Design and thermal performances of a scalable linear Fresnel reflector solar system. *Energy Conversion and Management*, 2017, 146:174–181.

[19] Mokhtar G, Boussad B, Noureddine S. A linear Fresnel reflector as a solar system for heating water: theoretical and experimental study. *Case Studies in Thermal Engineering*, 2016, 8:176–186.

[20] Bellos E, Tzivanidis C, Papadopoulos A. Daily, monthly and yearly performance of a linear Fresnel reflector. *Solar Energy*, 2018, 173:517–529.

[21] Xu G, Song G, Zhu X, *et al*. Performance evaluation of a direct vapor generation supercritical ORC system driven by linear Fresnel reflector solar concentrator. *Applied Thermal Engineering*, 2015, 80:196–204.
[22] Zhu G, Wendelin T, Wagner MJ, *et al*. History, current state, and future of linear Fresnel concentrating solar collectors. *Solar Energy*, 2014, 103:639–652.
[23] Abbas R, Sebastián A, Montes MJ *et al*. Optical features of linear Fresnel collectors with different secondary reflector technologies. *Applied Energy*, 2018, 232:386–397.
[24] Grena R, Tarquini P. Solar linear Fresnel collector using molten nitrates as heat transfer fluid. *Energy*, 2011, 36:1048–1056.
[25] Barbon A, Bayon-Cueli C, Bayon L, *et al*. Investigating the influence of longitudinal tilt angles on the performance of small scale linear Fresnel reflectors for urban applications. *Renewable Energy*, 2019, 143:1581–1593.
[26] Barbon A, Barbón N, Bayon L, *et al*. Parametric study of the small scale linear Fresnel reflector. *Renewable Energy*, 2018, 116:64–74.
[27] Kincaid N, Mungas G, Kramer N, *et al*. An optical performance comparison of three concentrating solar power collector designs in linear Fresnel, parabolic trough, and central receiver. *Applied Energy*, 2018, 231:1109–1121.
[28] Beltagy H. The effect of glass on the receiver and the use of two absorber tubes on optical performance of linear Fresnel solar concentrators. *Energy*, 2021, 224:120111.
[29] Bellos E, Tzivanidis C. Concentrating solar collectors for a trigeneration system—a comparative study. *Applied Sciences*, 2020, 10:4492.
[30] Biboum AC, Yilanci A. Thermodynamic and economic assessment of solar thermal power plants for Cameroon. *ASME The Journal of Solar Energy Engineering*, 2021, 143:041004.
[31] Ghodbane M, Boumeddane B, Said Z, *et al*. A numerical simulation of a linear Fresnel solar reflector directed to produce steam for the power plant. *Journal of Cleaner Production*, 2019, 231:494–508.
[32] Tuma PE. Fluoroketone $C_2F_5C(O)CF(CF_3)_2$ as a heat-transfer fluid for passive and pumped 2-phase applications. In: *Proceedings of the 2008 Twenty-fourth Annual IEEE Semiconductor Thermal Measurement and Management Symposium*, San Jose, CA, USA, 16–20 March 2008.
[33] Therminol. *Heat Transfer Fluids by Eastman*. https://www.therminol.com/about-eastman (29 April 2021, date last accessed).
[34] NREL. *System Advisor Model (SAM)*. https://sam.nrel.gov/ (13 May 2021, date last accessed)
[35] *Archimede Solar Energy (ASE)*. http://www.archimedesolarenergy.it/en_prodotti.htm (29 April 2021, date last accessed).
[36] Mahkamov K, Manca P, Mintsa A, *et al*. Development of a small solar thermal power plant for heat and power supply to domestic and small business buildings. In: *Proceedings of the ASME 2018 Power and Energy Conference*, Lake Buena Vista, Florida, USA, 24–28 June 2018.
[37] Synopsys. *LightTools Illumination Design Software*. https://www.synopsys.com/optical-solutions/lighttools.html (11 May 2021, date last accessed).
[38] Pino FJ, Caro R, Rosa F, *et al*. Experimental validation of an optical and thermal model of a linear Fresnel collector system. *Applied Thermal Engineering*, 2013, 50:1463–1471.
[39] Forrest EC, Hu LW, Buongiorno J, *et al*. Pool boiling heat transfer performance of a dielectric fluid with low global warming potential. *Heat Transfer Engineering*, 2013, 34:1262–1277.
[40] Hossin K, Mahkamov K, Belgasim B. Dynamic modelling of a small-scale standalone solar organic Rankine cycle system. In: *Proceedings of the 4th International Conference on Nuclear and Renewable Energy Resources*, Antalya, Turkey, 26–29 October 2014.
[41] Hossin K, Mahkamov K, Hashem G. Comparative assessment of working fluids for a low-temperature solar organic Rankine cycle power system. In: *Proceedings of the 2nd International Conference on Advances in Mechanical Engineering*, Istanbul, Turkey, 10–13 May 2016, 830–836.